International Journal of Scientific Advances
ISSN: 2708-7972
Volume: 7 | Issue: 2 | Mar – Apr 2026 Available Online: www.ijscia.com
DOI: 10.51542/ijscia.v7i2.7

Research on the Synthesis and AOP Application of Mesoporous Titanium Dioxide/Iron Containing MOF Composite Materials

Sabuj Hossain & Huihui Mao*

College of Petrochemical Engineering, Changzhou University, Changzhou, China

E-mail: sabujhossain9255@gmail.com; maohuihui@cczu.edu.cn

*Corresponding author details: Huihui Mao; maohuihui@cczu.edu.cn

ABSTRACT

TiO_2 is a very critical semiconductor material, showing high photocatalytic, catalytic oxidation and other activities in the near ultraviolet zone And TiO_2 rich source, relatively low price, good acid and alkali resistance, nontoxic side effects, light resistance and chemical exposure, with a wide band gap energy, etc., is widely used in photo-catalysis, environmental protection treatment, sensor, chemical synthesis, separation, and other fields Fe MOFs offer precise control over pore size and internal environments, optimizing their functionality for various applications. The rich content of Fe in nature and the low proximity of Fe make it widely favored in various MOF materials. In this paper, the mesoporous titanium dioxide was prepared by the solvent free self-assembly method and subsequently recombined with the Fe MOFS material X-ray powder diffraction (XRD), Fourier transform infrared spectroscopy (FT-IR) spectroscopy, electron scanning microscopy (SEM) showed that the synthesized TiO_2/Fe-MIL-101 material has good crystallinity and pore structure. TiO_2/Fe MIL-101 served as an effective catalyst in the photocatalytic degradation of Rhodamine B (RhB). The experimental results show that 0.5:1 TiO_2/Fe MIL-101 in 30 mg PMS has the best catalytic performance in 50 ml RhB, stirring and light degradation rate achieved 99% within 15 minutes.

Keywords: titanium dioxide; MOF; photocatalysis; AOP

1 INTRODUCTION

Mesoporous materials are a new type of inorganic polymer functional catalytic material [1], which plays a crucial role in the adsorption, separation, and catalyzing of large molecules, which often struggle to react within the confined spaces of microporous zeolite molecular sieves, especially in catalytic reactions. Mesoporous materials in the catalytic field are extensively applied in fields such as biomedicine, gas sensors, energy storage conversion, and have enormous application potential. The demand for ordered and transition metal oxides has been steadily rising, driven by their exceptional physical and chemical properties, as well as their wide range of potential applications across various industries [2]. Mesoporous metal oxides offer significant advantages over traditional bulk and nano materials, including a larger specific surface area, an open pore system, precise control over pore size and morphology, and excellent thermal and chemical stability. Ordered mesoporous transition metal oxides hold immense potential across various fields, including catalysis, adsorption, sensor technology, lithium-ion batteries, supercapacitors, and drug delivery. Mesoporous materials are typically classified into two main types: silicon-based and non-silicon-based. Due to the inability of mesoporous silicon-based materials to complete catalytic oxidation reactions, low exchange energy, low acid hardness, and low acid concentration [3]. People have also begun to attach importance to some mesoporous non-silicon-based materials, especially non-silicon-based mesoporous oxide materials with special semiconductor characteristics. Ordered mesoporous metal oxides, with their ability to exhibit variable valence states, unlock new possibilities for mesoporous materials. Their unique properties pave the way for applications beyond what silicon-based mesoporous materials can achieve, expanding their potential across various fields. Therefore, they are currently the most concerned new type of mesoporous materials.

1.1 Mesoporous TiO_2

Due to the excellent chemical properties of TiO_2 materials [4]: high stability, light resistance, corrosion resistance, good catalytic activity, it can effectively promote some endothermic organic chemical reactions for rapid synthesis on the surface of TiO_2 [5]. TiO_2 also has a long-range ordered pore structure and a highly crystallized pore wall. The duration of the process of electrons entering the crystal from the inside of the original crystal to the outer surface of the Network covalent bonding is greatly shortened, which further leads to the improvement of photocatalytic activity. In addition, TiO_2 itself is absolutely non-toxic and safe for the human body, and its cost of use is usually relatively low.

Therefore, research on the application of photocatalytic treatment technology for this new nano material TiO_2 is currently very active. Nano TiO_2 has been applied in various fields such as gas-phase laser sensors, photocatalysts, optical lenses, and optical batteries, and has a very broad industrial application development prospect.

1.2 Synthesis of Mesoporous Metal Oxides

At present, there are different methods for synthesizing mesoporous titanium dioxide [6]. It can be roughly divided into chemical and physical methods. Common chemical methods include: sol-gel method, volatilization-induced self-assembly method, hydrothermal synthesis method, precipitation method, etc. Physical methods include the gas-phase condensation method and ball milling method [7]. For different reactions, the required synthesis steps, synthesis conditions, and experimental reagents are all different. In practical research and production processes, people are often not limited to using one synthesis method for synthesis, but combine multiple process methods to further improve the physical and chemical properties of synthetic materials or save production costs.

1.2.1 Sol-gel method

The sol-gel method mainly uses metal alkoxides as raw materials. First, the alkoxides are completely dissolved in organic solvents by stirring. Wait for the completion of the hydrolysis of the alcohol salt water before adding deionized water. Quickly stir to undergo a hydrolysis reaction. By appropriately controlling the stirring time, solution pH, raw material selection, solution concentration, reaction medium, and reaction temperature, the goal of controlling the hydrolysis rate of the alcohol salt water is achieved. After hydrolysis for a period of time, the alkyd solution is dried at a low temperature, and the gel is dried by carefully controlled temperature and humidity to get the final sample. However, the high hydrolysis rate of alcohols presents a significant challenge to control their hydrolysis rate, making it difficult to obtain particles with ideal shape and size characteristics.

1.2.2 Volatilization-induced self-assembly method

Volatile-induced self-assembly can be used to simulate the formation of ordered nanostructures of organic-inorganic hybrid material in nature. This is a fast, simple, and efficient method for synthesizing structured, ordered nanocomposites. The principle is to use block copolymers as templates and self-assemble with inorganic precursors under coulomb or hydrogen bond interaction to form organic-inorganic hybrid composite materials. Then, the block copolymers are calcined and decomposed to obtain mesoporous metal oxides. This method is mainly used for the preparation of mesoporous TiO_2 membranes.

1.2.3 Hydrothermal method

Hydrothermal synthesis is a chemical synthesis reaction using substances in aqueous solution under high temperature and pressure. The hydrothermal method can effectively reduce chemical reaction time and quickly and directly obtain and precipitate crystal samples in a semi-crystalline state. In order to effectively avoid the collapse of the molecular mesoporous crystal structure caused by the lack of crystalline samples during the subsequent sample research process, using various template catalysts for treatment. The advantages of the Hydrothermal synthesis method are: it can improve the reaction speed, replace some high-temperature Dry media reactions, produce products with good dispersion, high purity, easy control of particles, less pollution in the preparation process, low degree of agglomeration, etc. Ceramic powders produced through hydrothermal synthesis methods are low in pollutants and do not require high-temperature forging treatment, avoiding problems such as grain growth, shape defects, introduction of impurities, etc., in the combustion process. The drawbacks of hydrothermal synthesis are that they mostly use organic compounds of Ti or intermediate products that are difficult to generate as precursors, resulting in high production costs and complex processes.

1.3 AOP Application

Many environmental issues that currently arise need to be urgently addressed. For example, the extensive release of organic and inorganic pollutants has resulted in the contamination of both surface water and groundwater. But methods for dealing with environmental issues have also been developed; these methods can be categorized into physical methods (such as membrane filtration and sedimentation), chemical methods (such as advanced oxidation process (AOP) and coagulation), and biological methods (such as activated sludge and biofiltration). Advanced oxidation processes are driven by the free radicals generated by the reaction, and the substrate is treated through oxidation. AOPs encompass various techniques, including odor treatment, the Fenton method, photocatalysis, wet air oxidation, microwave-enhanced AOP, electrochemical oxidation, ultraviolet radiation, and hydrogen peroxide oxidation. Historically, AOPs have played a crucial role in wastewater treatment, soil remediation, and the detoxification of hazardous substances, making them essential tools for environmental protection. In recent years, AOP has expanded beyond its traditional uses, finding applications in diverse fields like healthcare, organic synthesis, and energy production [8].

Furthermore, the free radicals produced during the AOP reaction can partially or entirely break down complex organic pollutants, converting them into carbon dioxide, water, and inorganic ions. However, the potential formation of unpredictable by-products in AOP can restrict its broader application. Usually in AOP, oxidants typically serve as precursors, which can be activated to generate free radicals. Three traditional AOP, Fenton system, percarbonate based AOP system, and persulfate based AOP system were studied based on different oxidation precursors. To enhance the generation of active radicals in AOP, various activation methods are commonly employed, including hot metals, alkalinity, UV radiation, ultrasound, and transition metals.

1.3.1 Photocatalysis

Photocatalysis works by harnessing light energy to trigger chemical reactions, generating free radicals as photons interact with molecules in the solution. This process can be triggered by spreading a fine-particle semiconductor slurry into a liquid and exposing it to energy sources like ultraviolet light, effectively initiating the reaction. Some semiconductors used for photocatalysis include titanium dioxide, zinc oxide, and cadmium. Titanium ore stands out as one of the most promising and widely researched materials for photocatalytic oxidation. The oxidation process kicks off when solar or ultraviolet radiation hits the metal surface, creating electron-hole pairs. These holes then react with water molecules or hydroxyl ions, generating powerful hydroxyl radicals that drive the reaction forward. The electrons formed can reduce the oxygen at the metal electrode to form peroxide or Superoxide. These pores play a crucial role in oxidation, directly interacting with the substrate to generate reactive free radicals.

The recombination of electron-hole pairs lowers quantum yield, making it crucial to explore ways to minimize quantum losses and improve efficiency. Recent advancements in photocatalysis focus on refining titanium dioxide as a solar catalyst. Heterogeneous processes allow catalysts to be recovered and reused, while solar energy helps cut costs by boosting production and efficiency. Photocatalytic oxidation shows great promise for wastewater treatment, particularly in removing colorants. Additionally, it holds potential for pre-treating excess sludge and enhancing the biodegradability of liquid bioenergy substrates.

1.4 Iron-based materials for catalytic AOP

The ferrous ions in transition metal groups have been extensively researched for their remarkable efficiency, low cost, high efficiency, and easy control. It has been extensively applied to improve the performance of AOP systems. Iron ions in a uniform AOP system can freely interact with oxidants without significantly affecting mass transfer. However, there are some challenges to consider: (1) The activation efficiency of iron ions is highly dependent on water pH and composition, which can lead to issues like iron sludge buildup and interactions with organic compounds; (2) Determining the right amount of iron is tricky higher concentrations of organic matter require more iron ions, but too many can suppress free radicals instead of enhancing the process; (3) The catalyst recovery rate is low. As a result, developing cost-effective and stable iron-based catalysts remains a significant challenge for iron-based catalytic AOP systems.

1.4.1 Iron-based MOF materials

MOF materials are created through a coordination reaction between metal ions and organic ligands, and have well-organized crystal structures and large surface areas. They offer exceptional potential for various applications. Researchers have successfully synthesized more than 2,000 distinct MOF materials, expanding their potential for various applications. [9]. The pore size and shape of MOF materials are influenced by the specific metal ions and organic ligands used in their structure. This variability allows them to be tailored for a wide range of applications, including sensing, gas storage, catalysis, energy production, and environmental remediation. Iron-based MOF materials exhibit excellent properties and chemical versatility due to their eco-friendly nature, combined with their distinctive structural features [10].

Iron-based MOF materials are also used for catalytically removing various dyes in persulfate systems [11]. For instance, Orange G (OG) and Rhodamine B (RhB) can be effectively eliminated, demonstrating the efficiency of the process. Iron-based MOF materials have enhanced efficiency in removing pollutants [12]. This paper uses Fe MIL-101, 1:1 TiO_2/Fe MIL-101, 0.5:1 TiO_2/Fe MIL-101, and 1.5:1 TiO_2/Fe MIL-101 to adsorb and degrade Rhodamine B solution to compare and analyze the adsorption and degradation effects of iron-based MOF. Notably, during the reaction, the leaching of iron ions in iron-based MOFs is minimal and can be disregarded. Since the catalytic oxidation primarily follows a heterogeneous reaction mechanism, the catalyst remains stable and performs reliably even after multiple cycles.

2 EXPERIMENTS

2.1 Synthesis of Mesoporous TiO_2

This study utilizes tetrabutyl titanate (TBOT) as the primary raw material and employs a straightforward, solvent-free self-assembly approach to synthesize mesoporous TiO_2 through a quick, five-minute grinding process at room temperature. The specific experimental plan is to place 0.45 g of PEI, 1 mL of glacial acetic acid, and 1.7 g of tetrabutyl titanate in a mortar and grind them manually for 5 minutes. PEI is a light-yellow viscous liquid that readily blends and reacts with tetrabutyl titanate and acetic acid. After grinding at room temperature for 5 minutes, it can form a uniform composite material. The composite material underwent calcination in a muffle furnace at 450°C for four hours, resulting in the formation of a highly crystalline mesoporous TiO_2 product.

The main advantages of using a solvent-free assembly strategy [14] to prepare mesoporous TiO_2 are as follows: (1) no solvent is required. Avoiding the use of solvents during the synthesis process not only reduces the generation of pollutants in line with the green chemical concept, but also reduces the consumption of energy and materials, saving production costs. (2) The synthesis process is simple, and the synthesis cycle is short. A simple and efficient solvent-free self-assembly approach allows inorganic oligomers and PEI to combine through hand grinding in a mortar at room temperature, completing the process in just five minutes. Compared with other synthesis schemes, the synthesis cycle only takes about 20 hours, which saves time and costs and is convenient to operate. (3) The target product yield is high. Due to the use of manual grinding and rapid solvent-free self-assembly strategies, compared to

other production processes, expected higher product yields, and yields can be achieved, which is more cost-effective. (4) Significantly reduce production costs. This scheme uses PEI for the synthesis of MMOs. As a cheap cationic polymer, PEI is usually sold in aqueous solutions with a concentration of 20% to 50%. Compared with block copolymers and surfactants, its price is much lower, greatly saving production raw material costs. (5) It also has good porosity and high crystallinity. Under high-temperature calcination at 450 ℃, the leftover PEI molecules act as stabilizers, helping to preserve the structural integrity and stability of mesoporous metal oxides (MMOs), resulting in high crystallinity and maintaining porosity. (6) This method is universally applicable. Due to the fact that this scheme only needs to pay attention to the toxicity of PEI and the safety at high temperatures of 450 ℃, the reaction conditions are simple and convenient compared to other schemes, and it can be widely used in experimental research and factory production.

2.2 Synthesis of Fe-MOF-101 Materials

The synthesis of iron-based MOF materials is mainly carried out by the hydrothermal method [15]. Hydrothermal method [16] uses hydrocolloid as the main reaction medium in a special sealed reaction vessel, and then uses Water heating to heat the reaction vessel to provide a high temperature and high-pressure reaction condition, so that ordinary insoluble or insoluble reaction materials can be completely dispersed in the hydrothermal medium, and then combined to form a well crystallized high-purity powder product after nucleation, and then centrifugation, water washing. Compared to other ways of preparing powder, hydrothermal synthesis, which includes drying and other post-treatment steps, offers several key advantages: (1) In most cases, crystalline powder can be produced directly without needing high-temperature sintering. This helps prevent grain growth, defects, and contamination that usually happen during calcination, resulting in powder with excellent sintering activity. (2) By tweaking the reaction conditions during the hydrothermal process, it's possible to control the crystal structure, shape, and purity of the nanoparticles. (3) Cheaper raw materials can be used. (4) Easy to obtain suitable stoichiometry and crystal shape advantages. Shortcomings of the hydrothermal method: Typically, only oxide powders can be produced, and there hasn't been much research into how to control the factors that influence nucleation and crystal growth.

The specific steps for the synthesis of iron-based MOF material [17] are as follows (See Table 2.3.1): weigh 1.35 g ferric chloride hexahydrate and 0.412 g terephthalic acid, mix them together, add them to 30 ml of di N-Methylformamide (DMF), mix them with ultrasonic stirring for 15 min, magnetic stirring for 30 min, and then react with each other under 110 ℃for 20 hours. To obtain iron-based MOF products, all samples underwent three rounds of centrifugal washing with DMF, followed by three additional washes with anhydrous ethanol. Finally, they were vacuum-dried at 80°C for several hours to ensure purity and stability.

2.3 Synthesis of TiO_2/Fe MOF-101 Materials

After consulting the literature, calculate the dosage of TiO_2 for three different ratios, which are 0.199 g for the 0.5:1 ratio, 0.3988 g for the 1:1 ratio, and 0.5965 g for the 1.5:1 ratio. Compared with the Fe MIL-101 material, when synthesizing TiO_2/Fe MIL-101, the number of other reagents remains unchanged; only the amount of TiO_2 is changed (Specific steps are shown in Table 1).

TABLE 1: Synthetic Proportions of Different Iron-Based MOF Materials.

	Fe MIL-101	1: 1TiO_2 / Fe MIL-101	0.5:1 TiO_2 / Fe MIL-101	1.5:1 TiO_2 / Fe MIL-101
Mesoporous TiO_2	nothing	0.3988 g	0.199 g	0.5965 g
$FeCl_3 \cdot 6H_2O$	1.3559 g	1.3591 g	1.35 g	1.35 g
H_2BDC	0.4121 g	0.4124 g	0.412 g	0.412 g
DMF	30 ml	30 ml	30 ml	30 ml
Ultrasonic stirring for 15 minutes, magnetic stirring for 30 minutes, transfer to a hydrothermal reactor, and hydrothermal reaction at 110 ℃for 20 hours.				
DMF centrifugal washing three times, anhydrous ethanol centrifugal washing three times, vacuum drying at 80 ℃for 20 hours.				

2.4 Characterization methods

Researchers use a range of techniques to study and better understand the physical and chemical properties of materials, facilitating the next experimental research on material applications [18]. In this paper, the prepared mesoporous TiO_2, iron-based MOF, TiO_2/Fe-MIL-101 composites were characterized and analyzed by means of X-ray powder diffraction (XRD), Fourier transform infrared spectroscopy (FT-IR), electron scanning microscope (SEM), specific surface area test (BET), thermogravimetric analysis (TG), and XPS analysis.

2.4.1 Field emission Scanning electron microscope (SEM)

Field emission Scanning electron microscope [19] is a precision instrument used to analyze the morphology of high-resolution micro areas. Its greatest strength lies in its ultra-high resolution, clear and intuitive imaging, impressive depth perception, and enhanced

relaxation properties. In this experiment, SEM (Zeiss Gemini 300, Germany) was mainly used to observe the crystal structure and morphology characteristics of mesoporous TiO_2 and iron-based MOF materials.

2.4.2 Fourier transform infrared spectroscopy (FT-IR)

The Fourier transform infrared spectrometer is abbreviated as the Fourier infrared spectrometer [20]. Each chemical molecule has a different basic structural composition and chemical structure, as well as its own unique infrared and absorption radiation spectra. By analyzing the infrared spectra, the basic structure of these chemical molecules can be scientifically analyzed and accurately identified. The infrared spectrometer model used in this experiment is PROTEGE. Using KBr as the background reference for five samples, mix trace amounts of products into an appropriate amount of KBr powder, grind evenly to powder form, and measure by pressing the tablet.

2.4.3 X-ray powder diffraction (XRD)

By irradiating the sample with high-energy X-rays, it gets excited to produce secondary fluorescence X-rays [21]. Qualitative analysis of the compound can be carried out by determining the diffraction angle position (peak position). In this experiment, Cu K was used α the peak values of five samples were analyzed by Diffractometer (Panalytical X'Pert3 Powder, Netherlands, wide-angle: 5~80 ° scanning speed 10 °/min).

2.4.4 Specific Surface Area Test (BET)

Materials that are highly porous, with an expansive surface area, exceptional reactivity, and powerful adsorption abilities, are poised to be incredibly useful across various applications. This article uses the BET method [22] to determine the corresponding specific surface area of five samples on the Micromeritics Tristar II 3020 instrument in the United States.

2.4.5 Thermogravimetric analysis (TG)

Thermogravimetric analysis is a method to keep the sample under the control of a certain temperature program and record the weight of the measured object as a function of time or temperature [23]. Thermogravimetric analysis is a powerful tool for assessing how materials hold up under different atmospheric conditions, providing insights into their thermal and oxidation stability. In this paper, the Thermogravimetric analysis (TGA) data is measured by TG 209F3 analyzer, with the temperature range of 30-800 ℃and the heating rate of 10 ℃· min − 1. The characterization analysis is carried out in combination with five characterization methods of XRD, BET, FI-IR, and SEM.

2.4.6 XPS Analysis

X-ray photoelectron spectroscopy (XPS) is a surface-sensitive analytical technique used to determine the elemental composition, oxidation states, and chemical bonding environments of materials. By measuring the binding energies of core electrons, XPS provides insights into the electronic structure and interactions between elements at the surface. This information is essential for understanding charge transfer behavior, surface reactivity, and the overall functionality of photocatalytic or composite materials.

2.5 AOP Application Experimental Steps

2.5.1 Experimental steps for the application of the composite sample Fe-MIL-101

In this paper, 10 mg of Rhodamine B is weighed into a beaker, added with distilled water, dissolved by ultrasound, transferred to a 1 L Volumetric flask, and the volume is fixed. The obtained solution is spectrophotometrically determined, and the value is taken as the initial value A0. Five kinds of materials, namely mesoporous TiO_2, Fe MIL-101, 1:1 TiO_2/Fe MIL-101, 0.5:1 TiO_2/Fe MIL-101, and 1.5:1 TiO_2/Fe MIL-101, are tested for the degradation of Rhodamine B solution, and the adsorption and degradation effects of iron-based MOF materials are compared and analyzed. Set only stirring (no light, no PMS added), stirring with light (no PMS added), and conducting application experiments on the best 0.5:1 TiO_2/Fe MIL-101 material among the five materials with 15 mg PMS, 20 mg PMS, 25 mg PMS, and 30 mg PMS stirring with light, respectively. The specific experimental content is as follows.

Stir only. Weigh 10 mg of the sample and 50 mL of Rhb solution respectively, put them in the sample bottle, turn on the Magnetic stirrer switch, take samples at an interval of 5 min, measure the spectrophotometric value of the samples, take six groups of samples in total, calculate the degradation rate, and make a chart record.

Stir and light. Weigh 10 mg of sample and 50 mL of Rhb solution respectively, put them in the sample bottle, turn on the Magnetic stirrer switch, turn on the xenon lamp light switch to simulate the light environment, take samples at 5 min intervals respectively, measure the spectrophotometric value of the samples, take six groups of samples in total, calculate the degradation rate, and make a chart record.

Mixing, lighting, and changing PMS dosage. Weigh 10 mg of sample, 50 mL of Rhb solution and 15 mg of PMS drug respectively into the sample bottle, turn on the Magnetic stirrer switch, turn on the xenon lamp light switch, take samples at 5 min intervals respectively, determine the spectrophotometric value of the samples, take six groups of samples in total, calculate the degradation rate, and make a chart record. Use the third method to determine the spectrophotometric values of the sample every 5 minutes at different PMS dosages of 20 mg, 25 mg, and 30 mg. Process each group of experimental data, calculate the degradation rate (see formula 2.5.1), and draw a degradation rate curve.

$$\eta = (A_0 - A_x) / A_0 \times 100\% \text{(公式2.5.1)}$$

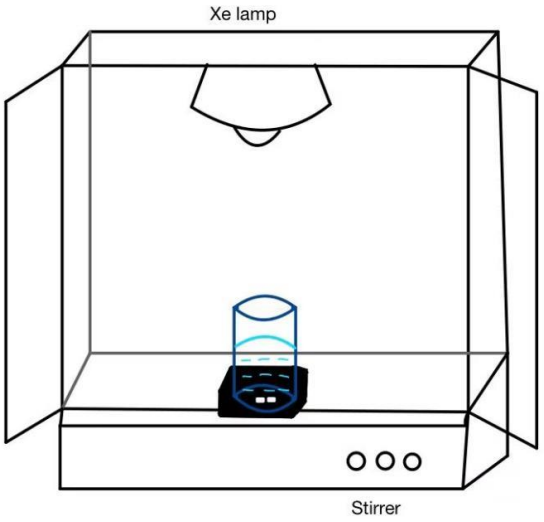

FIGURE 1: Photocatalytic reaction device diagram.

2.5.1 Quenching experiment

The occurrence of photocatalytic reactions relies on the excitation of electrons in the valence band of semiconductors by light radiation to the higher-level conduction band. This process leaves behind oxidizing holes in the valence band, while the excited electrons and these holes work together to drive subsequent redox reactions. However, in many cases, the redox degradation is not directly carried out by electrons or holes. Instead, electron holes first interact with electron acceptors or electron donors adsorbed on the surface of photocatalytic materials. This interaction leads to the formation of highly reactive intermediate substances, most of which are free radicals. These free radicals actively target specific structures within pollutant molecules, breaking them down through oxidative degradation. [24].

These free radicals can be roughly divided into the following categories [25]: hydroxyl radicals (· OH). A very common and highly active intermediate substance with strong oxidation ability; The reaction rate is fast, but its very short lifespan limits its diffusion distance, making it difficult to directly observe. The superoxide anion ($\cdot O_2^-$) is a common reactive substance, and in water, it basically behaves like a base. It can accept an H+ to form the protonated superoxide radical HOO ·. While HOO· isn't as reactive as other types of reactive oxygen species, it stands out because it lasts longer and can travel farther to reach its target location; its actual efficiency is still quite high. It can take place, such as disproportionation, single electron reduction reaction, single electron oxidation reaction, etc. Singlet oxygen. Singlet oxygen is just an oxygen molecule that's in a higher-energy, excited state, and the spin multiplicity is 1. This excited-state oxygen molecule also has strong oxidizability. However, in the process of photocatalysis, Oxygen molecules don't turn into singlet oxygen just by being exposed to light. Instead, a sensitizer needs to absorb the light first, get excited, and then pass that energy to the oxygen to create singlet oxygen. Some dyes are good sensitizers. Hydrogen peroxide. Sulfate radical (· SO 4-). It has almost the same oxidation capacity as that of · OH. Some studies have shown that the sulfate radical can exist for a longer time after it is generated, and its half-life can reach 4 s. This helps maintain longer contact with organic matter, boosting the breakdown process and allowing oxidation to last longer. Theoretically, under the same circumstances, the degradation degree of · OH will be increased, and the sulfate radical will also treat some organic matters that cannot be oxidized by the hydroxyl radical itself, Wider removal ability.

Under certain specific conditions, chlorine radicals, nitro radicals, etc., will also be discussed, but in conventional degradation reactions in pure water, photocatalytic degradation is generally discussed, including HOO·, ·OH, holes, singlet oxygen, hydrogen peroxide, etc.

In general, Electron paramagnetic resonance (ESR), fluorescence Notation [26], quenching, and other methods are used to study which free radicals are produced in the photocatalytic degradation system, what role they play, and the contribution of each free radical to degradation. When using the quenching method for analysis, although it is necessary to consider the addition of substances that may affect other active substances while quenching one free radical, the experimental operation is simple, manpower and materials are saved, and the experimental conclusions are relatively reliable. The principle of the quenching experiment is to select some species that are prone to free radical activity, and rely on substances that can specifically bind to free radicals and obtain stable products to quench free radicals and prevent them from exerting their original functions. The specific experimental method is to add specific quenching agents during the photocatalytic degradation process and observe whether the degradation rate decreases. If the degradation rate decreases to a greater extent, it indicates that the contribution of this free radical in the degradation process is higher.

In this paper, the quenching experiment method was used, and the hole quenching agent (methanol, Ammonium oxalate),· OH quenching agent (Tert-Butyl alcohol), electronic quenching agent (Potassium dichromate), singlet oxygen quenching agent (L-nenenebd histidine), and ·O_2 quenching agent (p-benzoquinone) were used for experiments. Weigh 10 mg, 50 mL RhB solution, 30 mg PMS of the sample with the best effect in the experiment of degrading Rhodamine B solution, respectively, and μ L methanol, 47 μ L Tert-Butyl alcohol, 147 mg Potassium dichromate, 62 mg oxalic acid, 77.58 mg Histidine, and 54 mg p-benzoquinone reagent were quenched under the condition of light and stirring, and samples were taken every 5 minutes to determine the sample spectrophotometric value. A total of 6 groups were sampled.

3 RESULTS AND DISCUSSION

3.1 Characterization analysis

3.1.1 SEM analysis

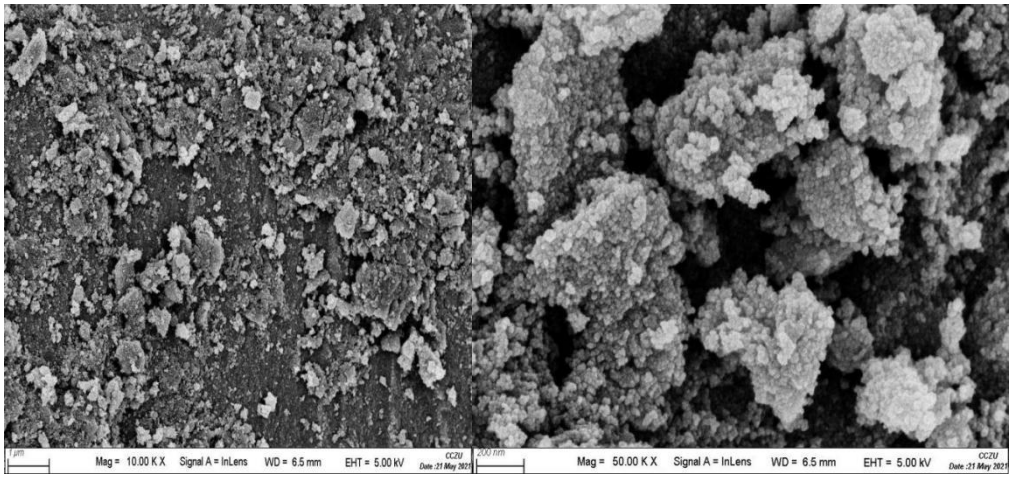

FIGURE 2: Scanning electron microscopy of mesoporous TiO_2.

Figure 2 (left) shows a mesoporous TiO_2 electron microscope 1 μ the scanning image of m, Figure 2 (right) shows the scanning image of mesoporous TiO_2 electron microscope at 200 nm (magnified 5x). From the grayscale area of the image (left), it can be seen that mesoporous titanium dioxide has a pore structure. From the enlarged image (right), it can be seen that the pore channels of titanium dioxide are large and dense, but the surface is rough [27], the crystal particles are irregular, and the surface has many vacancies, making it easy to composite with other materials.

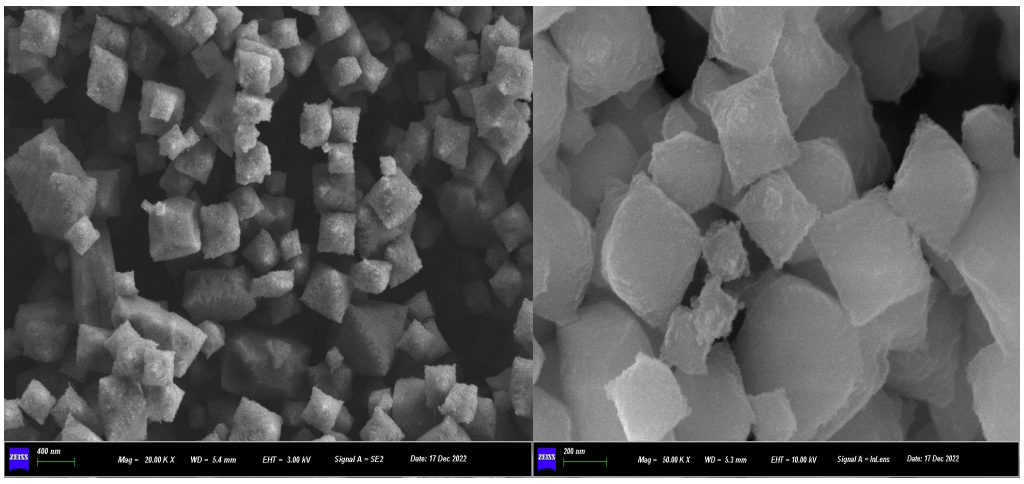

FIGURE 3: Scanning Electron Microscope of Fe MIL-101 Material.

Figure 3 (left) shows the scanning image of the Fe MIL-101 electron microscope at 400 nm, while Figure 3 (right) shows the scanning image of the Fe MIL-101 electron microscope at 200 nm (magnified twice). From the grayscale area in the figure (left), This shows that Fe-MIL-101 has a pore structure, and the particles are cubic crystals. From the enlarged image (right), this shows that the pore size of Fe-MIL-101 is smaller than that of TiO_2, but the surface is smoother [28], and the crystal particles are stacked more regularly.

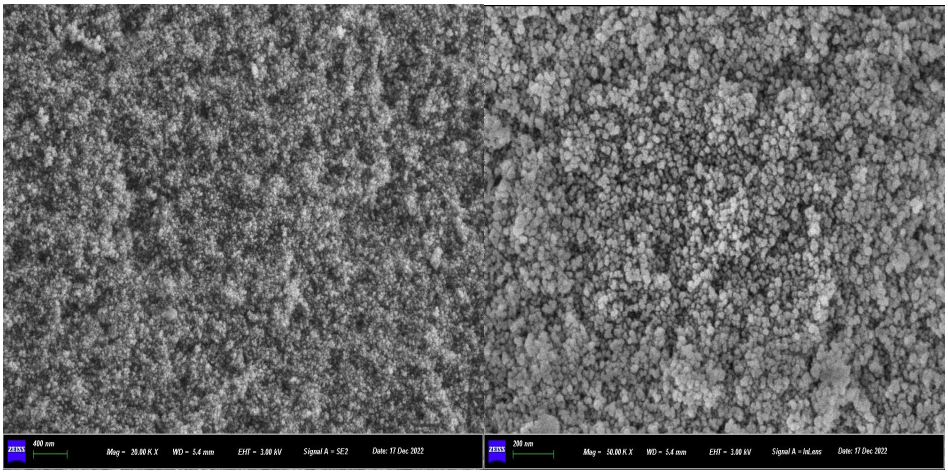

FIGURE 4 : Scanning electron microscopy of composite TiO_2/Fe MIL-101 material.

Figure 4 (left) shows the scanning image of the composite TiO_2/Fe MIL-101 electron microscope at 400 nm, and Figure 4 (right) shows the scanning image of the composite TiO_2/Fe MIL-101 electron microscope at 200 nm (magnified twice). From the grayscale area in the figure (left), this shows that the surface particles of the composite sample Fe-MIL-101 are very dense, forming a dense network structure. From the enlarged image (right), this shows that the pores of the composite sample Fe-MIL-101 are small but dense, with spherical particles on the surface [29].

3.1.2 FI-IR analysis

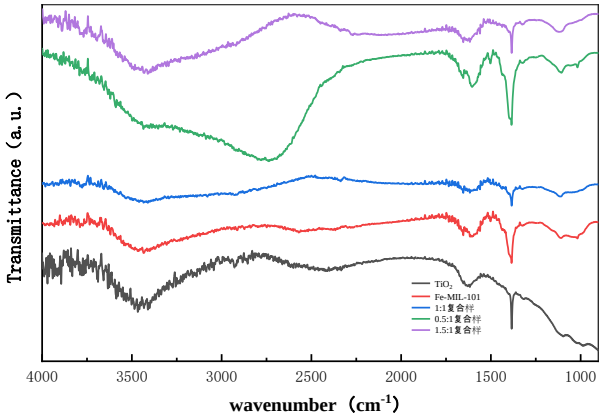

FIGURE 5: Infrared Spectra of Mesoporous TiO_2 and Composite TiO_2 Fe-MIL-101 Materials.

The figure clearly shows that all five samples share the same absorption peak at 1250-1500 cm-1. Unlike the other four samples, the best 0.5:1 composite sample has a larger absorption peak of 2750-3000 cm-1 than the other samples. There are small absorption peaks in the composite sample and iron-based MOF sample at 1129 cm-1, indicating the presence of Fe O groups. The absorption peak at 1350 cm-1 is the presence of 0-C=O groups. Due to measurement and operational errors, compared with standard infrared spectra, the C-O and C-H absorption peaks are relatively fine, around 1000 cm-1. The Ti-O bond absorption peak of mesoporous titanium dioxide is approximately 960 cm^{-1}.

3.1.3 XRD analysis

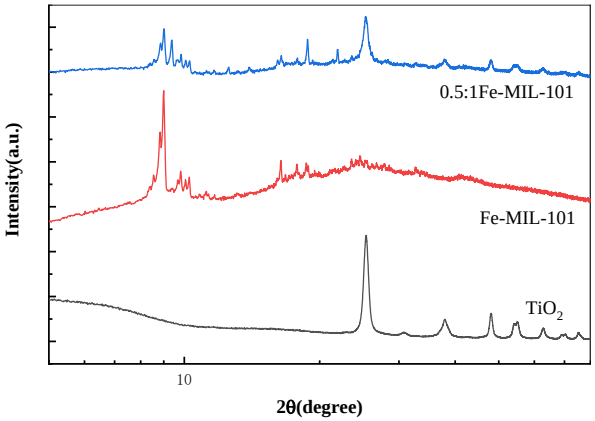

FIGURE 6: X-ray powder diffraction patterns of mesoporous TiO_2 and composite TiO_2/Fe MIL-101 samples.

Figure 6 shows the X-ray powder diffraction patterns of mesoporous titanium dioxide, Fe-MIL-101, and 0.5:1 TiO_2/Fe-MIL-101. From the X-ray powder diffraction pattern of mesoporous TiO_2, it can be seen that at 2Theta=25.3 °, 37.9 °, 48.1 °, 55.2 °, 62.8 °, 68 A characteristic peak appears at 75.2 °. The standard peak of PDF # 71-1166 is basically consistent with the standard card, and the XRD diffraction peak of mesoporous titanium dioxide is strong, indicating that the synthesized mesoporous TiO_2 has good crystallinity. The X-ray powder diffraction pattern of Fe-MIL-101 exhibits diffraction at 2Theta=8.99 °, 9.1 °, 16.4 °, and other locations. The characteristic peaks behind are small and dense.

The X-ray powder diffraction pattern of 0.5:1 TiO_2/Fe MIL-101 exhibits characteristic peaks similar to pure Fe MIL-101 at 2Theta=8.9 °, 18.9 °, 21.9 °, and the same diffraction peaks as mesoporous TiO_2 at 25.7 °, 37.5 °, 48.3 °, 54.3 ° 62.8 °. Therefore, it can be inferred that the sample at this ratio retains the structure of Fe MI 101 well and combines with the main structure of the raw TiO_2 [30].

3.1.4 Specific surface area properties

To compare and study the specific surface area and pore size changes of mesoporous TiO_2, Fe-MIL-101, and composite TiO_2/Fe MIL-101, the prepared catalyst samples were characterized by nitrogen adsorption and desorption curves, and the results are as follows.

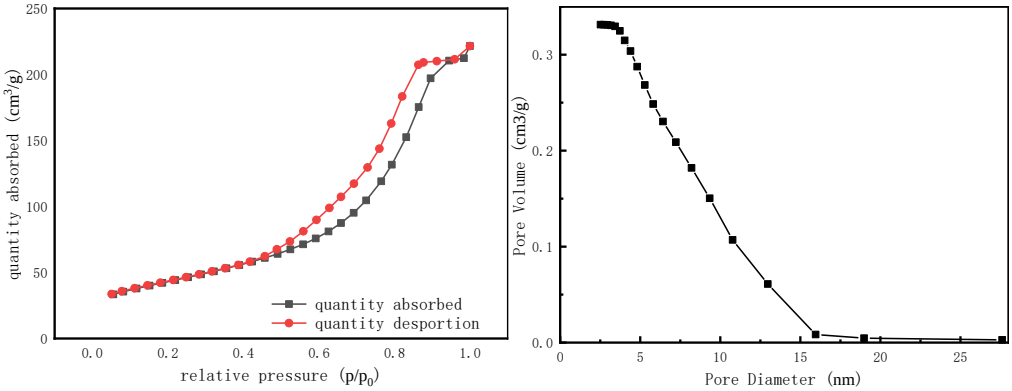

FIGURE 7: Nitrogen adsorption and desorption Contour line#Temperature and related subjects diagram (left) and pore size distribution diagram (right) of mesoporous TiO_2.

Figure 7 (left) shows the nitrogen adsorption-desorption Contour line#Temperature and related subjects of mesoporous TiO_2, and Figure 7 (right) shows how the pore sizes are distributed in mesoporous TiO_2. The figure shows that the nitrogen adsorption-desorption Contour line#Temperature and related subjects of mesoporous TiO_2 are between III and IV. This indicates the presence of a mixed hysteresis loop with H_2 (b). When P/P_0 is between 0.5 and 0.8, it is a saturated adsorption platform, reflecting a uniform pore size distribution. The adsorption curve indicates that mesoporous TiO_2 materials have certain pores. This matches what we see in the SEM image. From the pore size distribution map, we can see that the pore volume and size of the mesoporous TiO_2 have decreased to some extent, which may be due to the instability of the small pore channels of TiO_2 and their collapse. Or the channel is blocked [31].

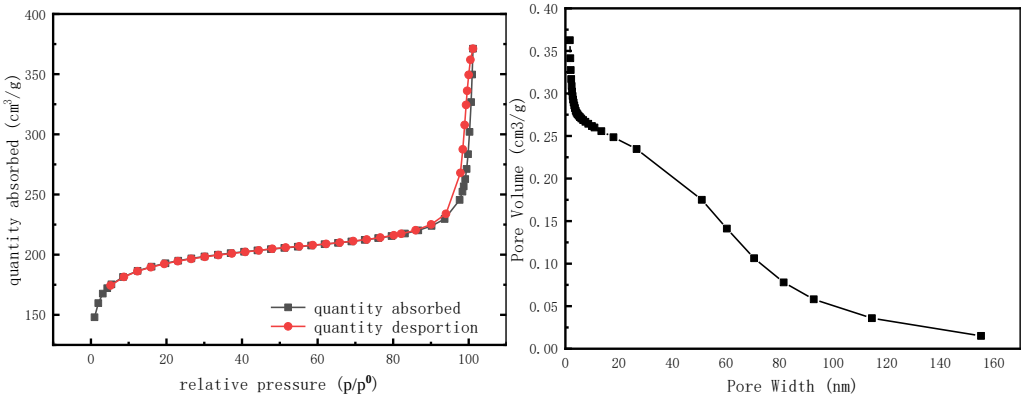

FIGURE 8: Nitrogen adsorption and desorption Contour line#Temperature and related subjects diagram of Fe-MIL-101 (left) and pore size distribution diagram (right).

Figure 8 (left) shows the nitrogen adsorption-desorption contour line#Temperature and related subjects of Fe-MIL-10, and Figure 8 (right) shows how the pore sizes are distributed in Fe-MIL-10. The figure shows that the nitrogen adsorption-desorption Contour line#Temperature and related subjects of Fe-MIL-101 is type III, there's a noticeable bend in the curve, marking the point where single-layer adsorption finishes. The absorption curve shows that the Fe-MIL-101 material has a microporous structure. The pore size distribution map shows a slight decrease in both pore volume and size, which might be caused by the accumulation or disappearance of small pores.

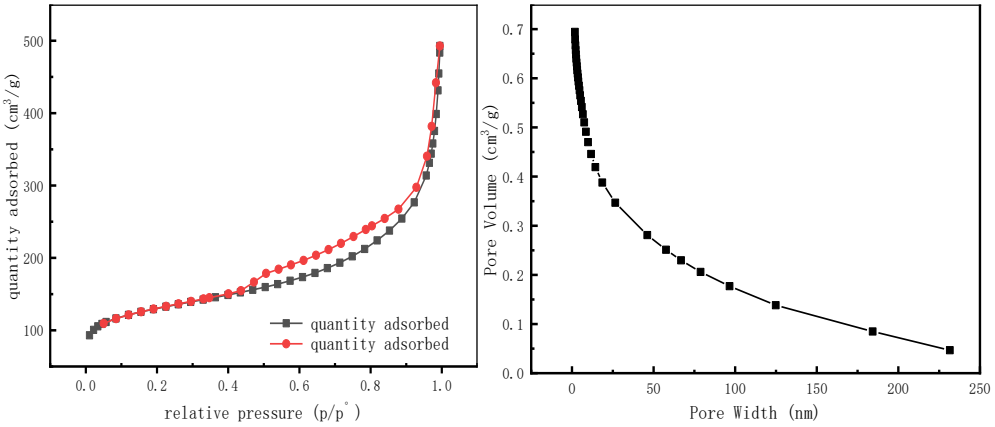

FIGURE 9: Nitrogen adsorption and desorption Contour line#Temperature and related subjects diagram (left) and pore size distribution diagram (right) of composite sample TiO_2/Fe-MIL-101.

Figure 9 (left) shows the nitrogen adsorption-desorption contour line#Temperature and related subjects of TiO_2/Fe-MIL-101, and Figure 9 (right) shows how the pore sizes are distributed in TiO_2/Fe-MIL-10. It can be seen from the figure that the nitrogen adsorption-desorption contour line#Temperature and related subjects of the composite sample is type III, but the knee curve in the figure is gentler (that is, it lacks a prominent inflection point), indicating that there is a single molecular layer of titanium dioxide covering.

To determine the specific surface area of the sample and the total volume of pores for single-point adsorption, the BET was used. Analyze the sample's average pore size using the BJH methodology. The results are shown in the table below.

TABLE 2: Specific Surface Area, Pore Capacity, and Pore Size Data of Materials.

Sample	Specific surface area (m^2/g)	Hole capacity (cm^3/g)	Average aperture (nm)
TiO_2	one hundred and fifty-four	zero point three four	eight point two nine
Fe MIL-101	six hundred and three	zero point six nine	nine point four five
TiO_2/Fe MIL-101	four hundred and sixty-two	zero point five zero	seven point five seven

The specific surface area and porosity of materials have an important impact on their chemical properties: generally speaking, the larger the specific surface area of materials, the more active sites and higher porosity can be provided, thus increasing the number of load sites of groups. From the table,

It's clear that the specific surface area of Fe-MIL-101 is 3.9 times that of mesoporous TiO_2, and that of the composite sample is 3 times that of TiO_2. The pore volume and pore size have also increased, while the specific surface area of the composite sample has decreased compared to Fe-MIL-101, indicating the accumulation and disappearance of pores.

3.1.5 Thermogravimetric analysis

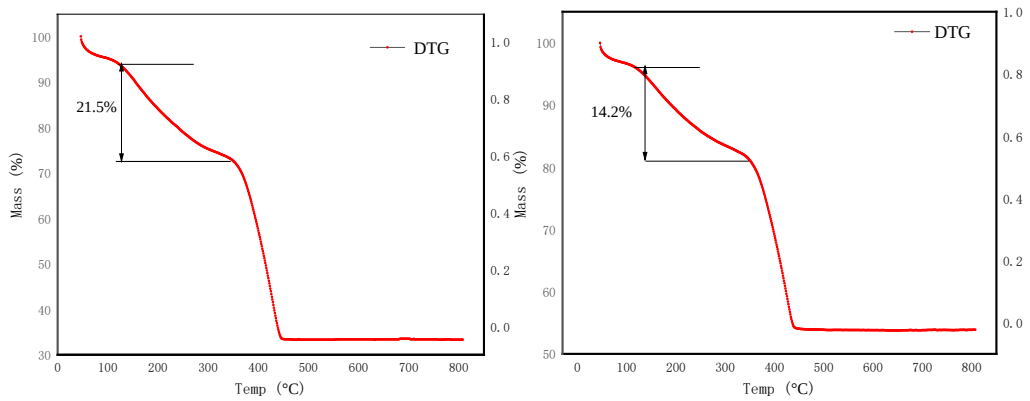

FIGURE 10: Thermogravimetric analysis of Fe-MIL-101 (left) and Composite Sample (right).

Figure 10 (left) shows that the total weight loss of Fe-MIL-101 is about 72%, while the total weight loss of TiO_2/Fe-MIL-101 composite sample in Figure 10 (right) is about 43%. In Figure 10 (left), the weight loss in the highly variable section is 21.5%, and the composite sample TiO_2/Fe MIL-101 is 14.2%. Compared to the two figures, the overall situation is similar, with a small range of water loss starting,

structural water loss in the curve section, and then organic matter decomposition. However, the thermal weight loss of the composite sample is much smaller than that of the Fe MIL-101 sample, indicating that the iron-based material structure after composite titanium dioxide is more stable [32].

3.1.6 XPS Analysis

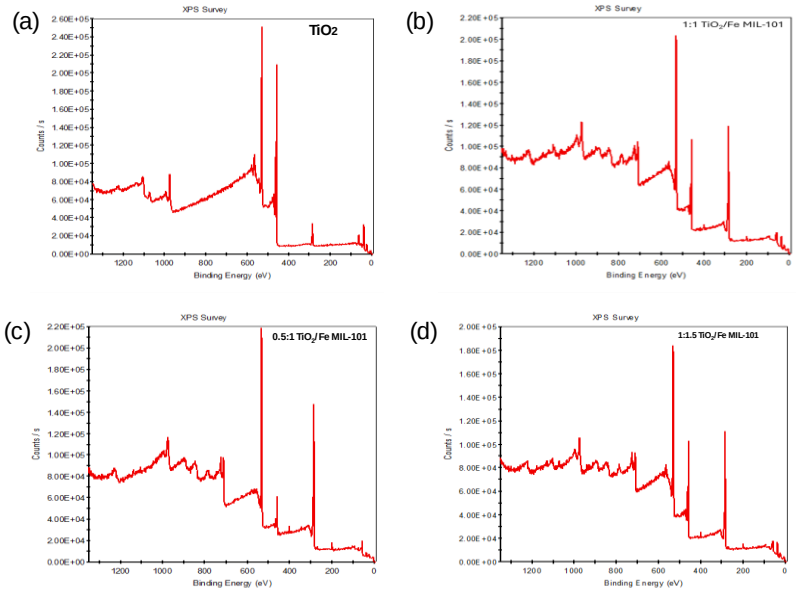

FIGURE 11 : (a) TiO_2, (b) 1:1 TiO_2/Fe MIL-101, (c) 0.5:1 TiO_2/Fe MIL-101, (d) 1:1.5 TiO_2/Fe MIL-101.

Figure 11 shows in Ti 2p, the binding energy of Ti^{4+} slightly shifts to higher values upon Fe-MOF addition, indicating Ti–O–Fe bond formation and a change in the Ti chemical environment. Fe 2p peaks at ~711 eV and ~724 eV confirm Fe^{3+} presence. A slight shift to lower energy in the composites suggests electron transfer from TiO_2 to Fe-MOF, confirming interfacial interaction. O 1s spectra show increased hydroxyl and adsorbed oxygen species in composites, especially at higher Fe content, supporting the formation of new chemical bonds and enhanced surface activity. The XPS results confirm heterojunction formation via Ti–O–Fe bonding and electron transfer between TiO_2 and Fe-MOF. This structure enhances charge carrier separation, reducing recombination and improving photocatalytic performance.

3.2 Analysis of application results

3.2.1 Mixing only

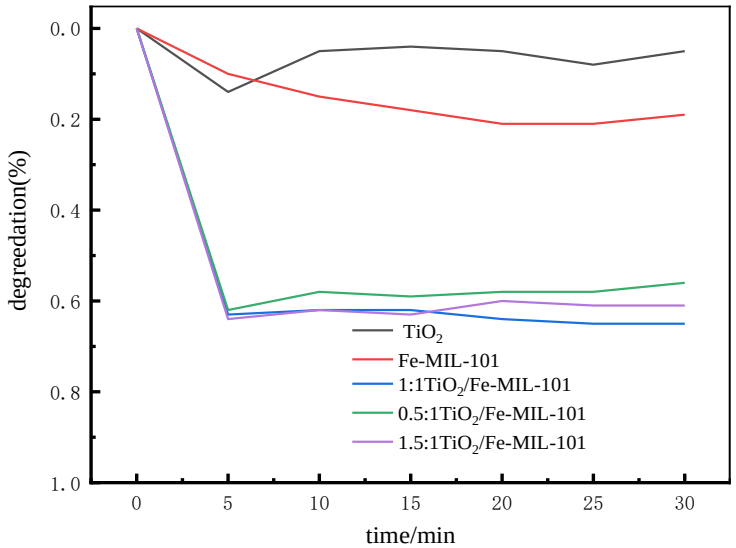

FIGURE 12: Degradation rate diagram of five samples under stirring conditions only.

From the degradation rate graph obtained by only stirring this set of experimental data processing, it can be seen that within the first five minutes, the degradation rate of the 1:1 TiO_2/Fe MIL-101, 0.5:1 TiO_2/Fe MIL-101, and 1.5:1 TiO_2/Fe MIL-101 composite samples were the fastest, followed by mesoporous TiO_2 and Fe MIL-101. After five minutes, the degradation of the composite samples in different proportions remained flat with little fluctuation, while mesoporous TiO_2 showed a slow degradation trend, and the pure Fe-MIL-101 material did not have a significant degradation effect.

Without turning on the light and adding PMS, the adsorption effect of the material was investigated. As shown in the figure, TiO_2 material had almost no adsorption effect on RhB, and only 8.2% of RhB was degraded after 30 minutes. Because of its high specific surface area and large pore size, Fe-MIL-101 has a strong adsorption effect and can adsorb 65.5% RhB in 30 minutes.

3.2.2 Mixing and lighting

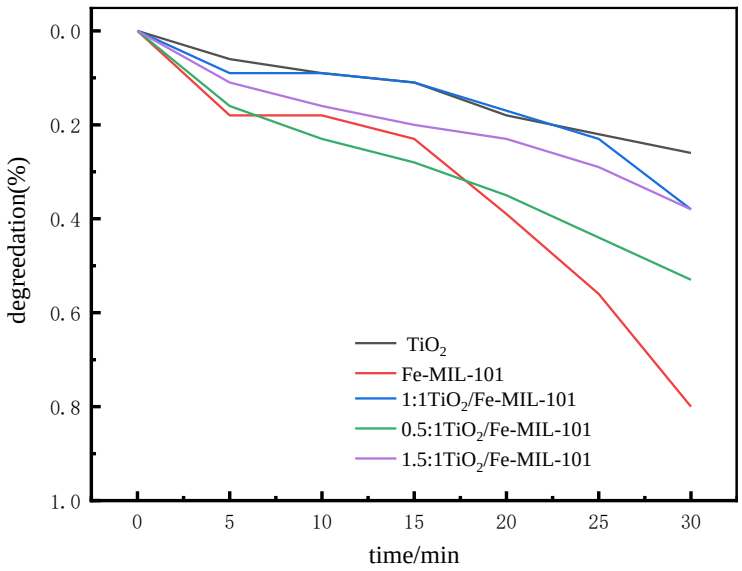

FIGURE 13: Degradation rate diagram of five samples under stirring and lighting conditions.

From the data processing chart of the experiment of mixing and lighting, it can be seen that the photocatalytic effect of the five samples is good, with Fe MIL-101 having the most obvious effect, reaching 82% after 30 minutes. Secondly, 0.5:1 TiO_2/Fe MIL-101 is the most effective composite sample among the three different ratios, reaching 53% after half an hour. The worst effect of mesoporous TiO_2 is only 20%.

3.2.3 Different dosages of PMS

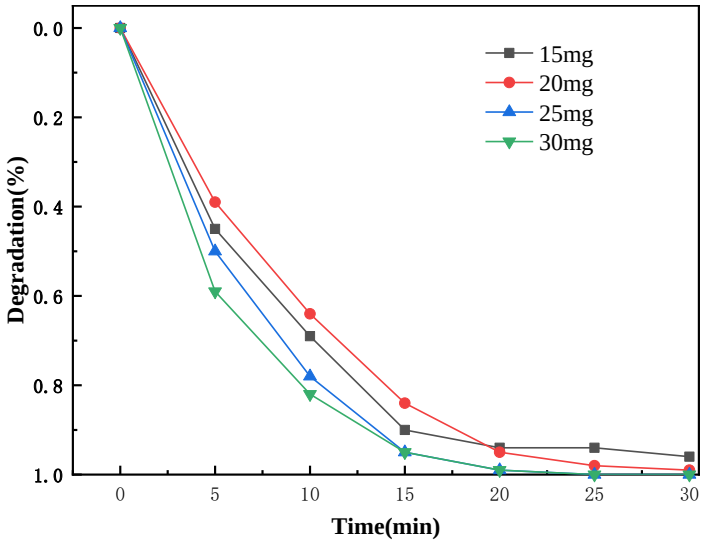

FIGURE 14: 0.5:1 TiO_2/Fe MIL-101 Decreasing Solution Rate under Different Doses of PMS Conditions.

Select the sample with the best effect in different proportions of composite samples, 0.5:1 TiO_2/Fe MIL-101, for comparative experiments with different doses of PMS. From the experimental graph after data processing, it's clear that the degradation effect is further improved after adding PMS, which can reach around 100% after 30 minutes. At 30 mg PMS, the degradation is fastest, followed by 25 mg, 15 mg, and 20 mg. It has been proven that PMS has a noticeable impact on the photocatalytic degradation of samples, but it is not that the more PMS dosage, the more effective it is, nor is it that the less effective it is. Further experimental exploration can be conducted on the optimal dosage of PMS.

3.2.4 Mixing with light and 30 mg PMS

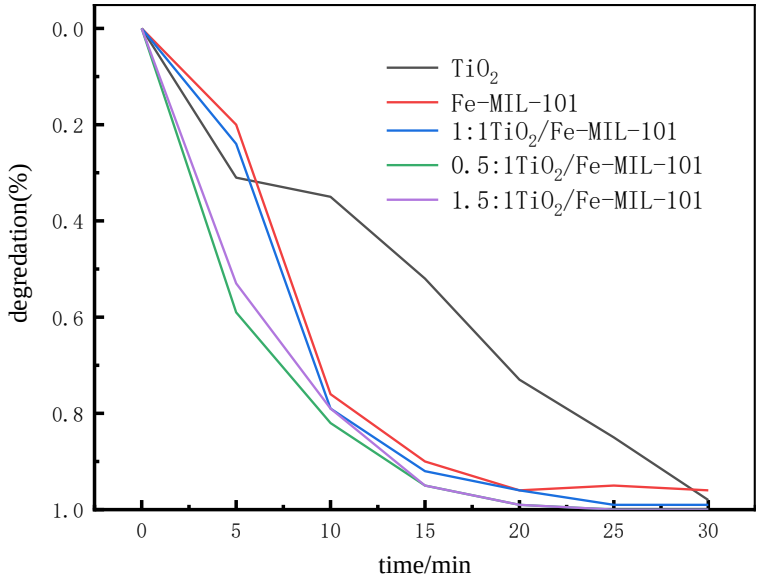

FIGURE 15: Degradation rate diagram of five samples under 30 mg PMS conditions.

From the experiments with different doses of PMS, it can be seen that 30 mg of PMS has the best effect. Under these conditions, five samples were tested separately. From the degradation rate graph, it's clear that the degradation effect of iron-based MOF materials is much better than mesoporous TiO_2, but after 30 minutes, all five samples can be basically degraded. The composite sample has the best effect among the five samples, with a ratio of 0.5:1 TiO_2/Fe - MIL-101 being the best among the three, reaching 100% after 15 minutes. From the figure, it can be assumed that the composite sample ratio can be set to 0.4:1 Fe MIL-101, 0.3:1 Fe MIL-101, and further experiments will be conducted to explore the best ratio.

3.2.5 Quenching experiment results

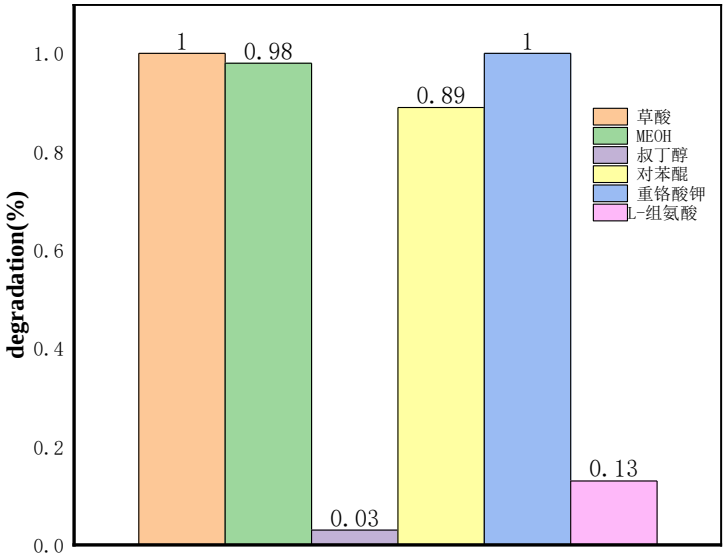

FIGURE 16: Degradation rate diagram of quenching experiment.

From Figure 16 of the quenching effect of free radicals, it can be seen that [33] potassium dichromate has almost no effect, indicating that the influence of electronic free radicals is relatively small, while singlet oxygen, · O_2−, h+, and · OH have some promotional effects on photo-Fenton degradation. With the supplementation of tert-butyl alcohol, the photo Fenton reaction was almost completely inhibited, and the degradation rate of RhB within 30 min was about 3%, followed by L-nenenebb histidine, which was 13%. Indicating that · OH and singlet oxygen are the main reactive substances at work in the system. The addition of p-benzoquinone also had a certain impact on the reaction, with a degradation rate of about 89%, indicating that · O_2− was also involved in the reaction. The inhibition rate of methanol and oxalic acid on the reaction is not high.

3.2.6 Degradation of Kinetics and Model Fitting

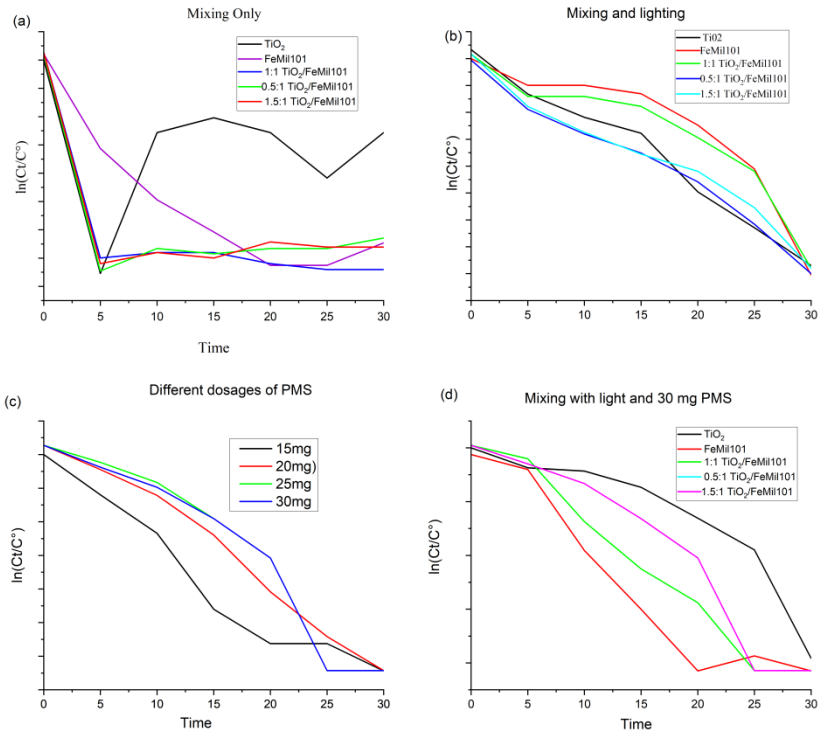

FIGURE 17: Degradation Kinetics and Model Fitting (a)Mixing Only, (b) Mixing and Lighting, (c)Different dosages of PMS, (d)Mixing with Light and 30mg PMS.

From Figure 17 (a), under dark conditions, negligible degradation was observed, indicating the necessity of light or oxidant activation. Upon light irradiation, Figure 17 (b), all samples showed a near-linear decline, with the 0.5:1 TiO_2/FeMIL-101 composite exhibiting the highest degradation rate.

As shown in Figure 17 (c), increasing PMS dosage significantly enhanced degradation, with higher doses generating more reactive radicals (SO_4^{-}· and ·OH). Under full activation (light + 30 mg PMS, Figure 17 (d), all composites achieved rapid RhB removal, with the 0.5:1 TiO_2/FeMIL-101 ratios outperforming.

3.2.7 ESR Analysis

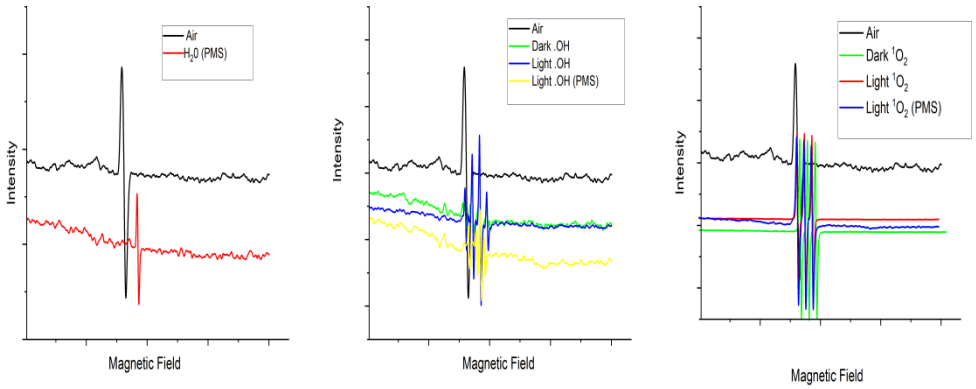

FIGURE 18 : EPR spectra showing radical generation.

EPR spectra of the catalyst system in the presence of spin-trapping agents (DMPO for ·OH, TEMP for $1O_2$) under various conditions. Stronger radical signals under light + PMS confirm the generation of active species, particularly ·OH and $1O_2$, verifying the synergistic effect between photocatalysis and PMS activation.

CONCLUSION

To sum up, we prepared mesoporous TiO2 through solvent-free self-assembly. After grinding 0.45 g of Polyethylenimine, 1 mL of acetic acid, and 1.7 g of tetrabutyl titanate and calcining at 450 ℃for 4 hours, mesoporous TiO2 was successfully prepared, and the specific surface area of the mesoporous TiO2 material was 153.8 m^2/ g.

The total volume of pores for single-point adsorption is 0.34 cm ^{3}/ g. The average pore size is 8.29 nm. Subsequently, a composite TiO2/Fe MIL-101 material was obtained by hydrothermal reaction of 0.39 g mesoporous TiO2 with 0.412 g H2BDC, 1.36 g FeCl3 · 6H2O, and 30 mL DMF at 110 ℃The five synthesized samples were compared and analyzed using five characterization methods. Finally, the composite sample TiO2 Fe MIL-101 was applied to AOP, and the results showed that the 0.5:1 TiO2/Fe MIL-101 catalyst had significant catalytic activity. The catalytic activity is best under reaction conditions of 30 mg PMS, 50 mL RhB solution, 10 mg sample, stirring, and light irradiation. The catalyst's activity depends on how much mesoporous TiO_2 is present. When the reagent dosage of mesoporous TiO2 is 0.5965 g, the catalytic effect of the composite TiO2/Fe MIL-101 catalyst obtained is not as good as that of the TiO2/Fe MIL-101 catalyst at the reagent dosage of 0.199 g.

The enhanced photocatalytic activity of TiO2/Fe MIL-101 is mainly attributed to the strong adsorption performance of Fe MIL-101 on RhB molecules, which greatly shortens the migration distance of active singlet oxygen, thereby improving catalytic performance.

REFERENCES

[1] Huang Liang. Preparation and Photocatalytic Performance of Titanium Dioxide Mesoporous Materials [D] Donghua University, 2009

[2] G W, Wang S Y, Zhong C, et al. Application of Fe MOFs in advanced oxidation processes [J] Research on Chemical Intermediates, 2019,45 (7): 3777-3793 DOI: 10.1007/s11164-019-03820-5

[3] Li Yuexiang, Lv Gongxuan, Li Shuben Photocatalytic reduction of Rhodamine B by Pt-TiO2 [J] Molecular catalysis, 2001,15 (4): 287-290 DOI: 10.3969/j.issn.1001-3555.2001.04.011

[4] LI, HUIHUI, NING, FUCHUN, CHEN, XIAOFEI, et al. Effect of carbon and nitrogen double vacances on the improved photocatalytic hydrogen evolution over polar carbon nitrate nanosheets [J]. Analysis science&technology, 2021,11 (9): 3270-3278 DOI: 10.1039/d0cy02453h

[5] Li Bing.Synthesis and adsorption properties of functionalized silicon-based mesoporous materials [D] Jiangsu: Nanjing University of Science and Technology, 2014. DOI: 10.76666/d.Y2521883

[6] Guo Liying. Preparation and characterization of mesoporous titanium dioxide [D]. Shaanxi: Shaanxi University of Science and Technology, 2010 DOI: 10.76666/d.y1799065

[7] He Zuoli. Morphological control and performance study of doped nano titanium dioxide [D] Shaanxi: Shaanxi University of Science and Technology, 2011. DOI: 10.76666/d.y1974256

[8] HESHAN ZHENG, YUNYING HOU, SHUO LI, et al. Study on catalytic mechanisms of Fe3O4-rGOx in three typical advanced oxidation processes for tetracycline hydrochloride degradation [J] China Chemical Express (English version), 2023,34 (1): 420-425

[9] Li, Wei, Jun Liu, and Dongyuan Zhao. "Mesoporous materials for energy conversion and storage devices." Nature Reviews Materials 1.6 (2016): 16023.

[10] Wei, Jing, et al. "New insight into the synthesis of large-pore ordered mesoporous materials." Journal of the American Chemical Society 139.5 (2017): 1706-1713.

[11] Crossland, Edward JW, et al. "Mesoporous TiO2 single crystals delivering enhanced mobility and optoelectronic device performance. " Nature 495.7440 (2013): 215-219.

[12] Jo, Changshin, et al. "Multiscale phase separations for hierarchically ordered macro/mesostructured metal oxides." Advanced Materials 30.6 (2018): 1703829.

[13] H. L. Xiong, T. N. Gao, Y. L. Liu, Y. L. Ma, J. W. Liu, Z. - A. Qiao, S. Y. Song, S. Dai, Adv. Sci June 2019, 1801543

[14] Hwang, Jongkook, et al. "Generalized access to mesoporous inorganic particles and hollow spheres from multicomponent polymer blends." Advanced Materials 30.27 (2018): 1801127.

[15] Poyraz, Altug S., et al. "A general approach to crystalline and monomodal pore size mesoporous materials." Nature Communications 4.1 (2013): 2952.

[16] Song, Guoqiang, et al. "Preparation of MOF (Fe) and its catalytic activity for oxygen reduction reaction in an alkaline electrolyte." Chinese Journal of Catalysis 35.2 (2014): 185-195.

[17] Brezesinski, Torsten, et al. "Ordered mesoporous α-MoO3 with iso-oriented nanocrystalline walls for thin-film pseudocapacitors." Nature Materials 9.2 (2010): 146-151.

[18] Teng Yujie, Wang Xingdan Characterization method for TiO2 photocatalytic efficiency [J] Chemical engineer, 2008,22 (2): 26-27,45 DOI: 10.3969/j.issn.1002-1124.2008.02.011

[19] An Guo Mang, Liu Xingping, Xie Yonghong, et al Scanning electron microscopy analysis of the morphology of domestic high-purity TiO2 powder particles [J] Journal of Electronic Microscopy, 2002,21 (5): 776-777 DOI: 10.3969/j.issn.1000-6281.2002.05.155

[20] Zhou Jianjun, Cui Haiping, Yan Jun Photocatalytic Performance and Infrared Spectral Analysis of Inorganic Anion Doped TiO2 Thin Films [J] Information Record Materials, 2006,7 (6): 10-13
DOI: 10.3969/j.issn.1009-5624-2006.06.003

[21] Chen Qili, Tang Chaoqun, Xiao Xun Preparation of TiO2 nanoparticles by sol-gel method and XRD analysis [J] Materials Science and Engineering, 2002,20 (2): 224-226
DOI: 10.3969/j.issn.1673-2812.2002.02.021

[22] Tao Yueqian, Ren Lu, Yang Mingyue, et al The effect of hydrothermal reaction hydrolysis rate on the photocatalytic performance of nano TiO2 [J] Printing and dyeing auxiliaries, 2023,40 (3): 35-40. DOI: 10.3969/j.issn.1004-0439.2023.007

[23] Yue Linhai, Liu Qing, Xu Zhunde, et al Preparation and characterization of nanometer iron doped titanium dioxide by sol-gel method (I) Thermal decomposition and crystallization characteristics of iron doped titanium dioxide gel analyzed by TG-IR [J] Journal of Inorganic Chemistry, 2000,16 (6): 933-938
DOI: 10.3321/j.issn: 1001-4861.2000.06.013

[24] Xiao, Weiming, et al. "Facile synthesis of highly porous metal oxides by mechanochemical nanocasting." Chemistry of Materials 30.9 (2018): 2924-2929.

[25] Deng, Xiaohui, Kun Chen, and Harun Tüysüz. "Protocol for the nanocasting method: preparation of ordered mesoporous metal oxides." Chemistry of Materials 29.1 (2017): 40-52.

[26] Luc, Wesley, and Feng Jiao. "Synthesis of nanoporous metals, oxides, carbides, and sulfides: beyond nanocasting." Accounts of chemical research 49.7 (2016): 1351-1358.

[27] Yen, Hoang, et al. "One-step-impregnation hard templating synthesis of high-surface-area nanostructured mixed metal oxides (NiFe 2 O 4, CuFe 2 O 4 and Cu/CeO 2)." Chemical Communications 47.37 (2011): 10473-10475.

[28] E. Pellicer, E. Rossinyol, P. Solsona, S. Suri č ach, M. Dolors Barl, J. Sort, Adv. Function Material 2013, 23, 900-911

[29] H. Yen, Y. Seo, S. Kaliaguine, F. Kleitz, Angelw Chem Int. Ed. 2012, 51, 12032-12035; Angelw Chem 2012, 124, 12198-12201

[30] Roggenbuck, Jan, Günter Koch, and Michael Tiemann. "Synthesis of mesoporous magnesium oxide by CMK-3 carbon structure replication." Chemistry of Materials 18.17 (2006): 4151-4156.

[31] Jiao, Feng, et al. "Mesoporous Mn2O3 and Mn3O4 with crystalline walls." Advanced Materials 19.22 (2007): 4063-4066.

[32] Sun, Xiaohong, et al. "Container effect in nanocasting synthesis of mesoporous metal oxides." Journal of the American Chemical Society 133.37 (2011): 14542-14545.

[33] Gu, Xin, et al. "Synthesis and microwave absorbing properties of highly ordered mesoporous crystalline NiFe 2 O 4." Chemical Communications 47.18 (2011): 5337-5339.